DOI: 10.1002/ ((please add manuscript number))
Article type: Communication

Single Cobalt Sites Dispersed in Hierarchically Porous Nanofiber Networks for Durable and High-Power PGM-free Cathodes in Fuel Cells

Yanghua He[1], Hui Guo[1], Sooyeon Hwang[1], Xiaoxuan Yang[1], Zizhou He, Jonathan Braaten, Stavros Karakalos, Weitao Shan, Maoyu Wang, Hua Zhou, Zhenxing Feng, Karren L. More, Guofeng Wang, Dong Su, David A. Cullen, Ling Fei*, Shawn Litster*, and Gang Wu**

Y. He, X. Yang, Prof. G. Wu
Department of Chemical and Biological Engineering,
University at Buffalo, The State University of New York,
Buffalo, NY 14260, USA.
E-mail: gangwu@buffalo.edu

H. Guo, Z. He, Prof. L. Fei
Department of Chemical Engineering,
University of Louisiana at Lafayette,
Lafayette, Louisiana 70504, USA.
E-mail: ling.fei@louisiana.edu

Dr. S. Hwang, Dr. D. Su
Center for Functional Nanomaterials,
Brookhaven National Laboratory,
Upton, NY 11973, USA

J. Braaten, Prof. S. Litster
Department of Mechanical Engineering,
Carnegie Mellon University,
Pittsburgh, PA 15213, USA.
E-mail: litster@andrew.cmu.edu

Dr. S. Karakalos
Department of Chemical Engineering,
University of South Carolina,
Columbia, SC 29208, USA

Dr. W. Shan, Prof. G. Wang
Department of Mechanical Engineering and Materials Science,
University of Pittsburgh,
Pittsburgh, PA 15261, USA

M. Wang, Prof. Z Feng
School of Chemical, Biological, and Environmental Engineering,
Oregon State University,
Corvallis, OR 97331, USA

Dr. H. Zhou
X-ray Science Division,

Argonne National Laboratory,
Lemont, IL 60439, USA

Dr. D. A. Cullen, Dr. K. L. More
Center for Nanophase Materials Sciences,
Oak Ridge National Laboratory,
Oak Ridge, TN 37831, USA.
E-mail: cullenda@ornl.gov

[1]These authors contributed equally.

Abstract. Increasing catalytic activity and durability of atomically dispersed metal-nitrogen-carbon (M-N-C) catalysts for oxygen reduction reaction (ORR) cathode in proton exchange membrane fuel cells (PEMFCs) remains a grand challenge. Here, we report a high-power and durable Co-N-C nanofiber catalyst synthesized through electrospinning cobalt-doped zeolitic imidazolate frameworks (ZIFs) into selected polyacrylonitrile (PAN) and polyvinylpyrrolidone (PVP) polymers. The distinct porous fibrous morphology and hierarchical structures play a vital role in boosting electrode performance by exposing more accessible active sites, providing facile electron conductivity, and facilitating the mass transport of reactant. The enhanced intrinsic activity is attributed to the extra graphitic N dopants surrounding CoN_4 moieties, which induced higher charge density on adjacent carbon atoms, therefore optimizing the activation energies of bond cleavage for the *OOH dissociation process and substantially increasing intrinsic ORR activity. The highly graphitized carbon matrix in the catalyst is beneficial for enhancing carbon corrosion resistance, thereby promoting catalyst stability. The unique nanoscale X-ray computed tomography (nano-CT) imaging highlighted the well-distributed ionomer coverage throughout the fibrous carbon network in the catalyst, thereby constructing effective three-phase boundaries (TPBs) for the ORR. The membrane electrode assembly (MEA) achieved a record-high power density of 0.40 W cm^{-2} in a practical H_2/air cell (1.0 bar) and demonstrated significantly enhanced durability under various accelerated stability tests. The combination of the enhanced intrinsic activity and stability of single CoM_4 sites, along with unique hierarchical catalyst architecture, provide new insight into designing efficient

PGM-free electrodes with improved performance and durability.

1. Introduction

Atomically dispersed and nitrogen coordinated single metal sites embedded in carbon (denoted as M-N-C) have emerged as promising platinum group metal-free (PGM-free) catalysts for the oxygen reduction reaction (ORR) cathode in proton-exchange membrane fuel cells (PEMFCs).[1-5] The MN_4 (M: Fe, Co, or Mn) moieties have been theoretically predicted and then experimentally verified as the active sites in M-N-C catalysts.[6-13] Among the many studied precursors, zinc-based zeolitic imidazolate frameworks (ZIF-8s) are effective in creating atomically dispersed MN_4 sites embedded in defect-rich carbon during the high-temperature carbonization.[8, 10, 14-17] Despite their encouraging ORR activity demonstrated in aqueous acidic electrolytes recently,[18] the trend is often difficult to reproduce in the membrane electrode assemblies (MEAs) of PEMFCs using solid-state electrolytes (*i.e.*, Nafion) (**Table S1**).[19] Low catalyst utilization, severe carbon corrosion, and inferior mass transport within the very thick PGM-free cathode catalysts layers (CCLs) are the primary limitations of MEA performance.[20, 21] In solid-state electrodes, the ORR ($O_2 + 4H^+ + 4e^- \rightarrow H_2O$) only occurs at the triple-phase boundary (TPB), where the gas (O_2) and protons (H^+) transported through the electrolyte phase (Nafion ionomer) coverage with electrons (e^-) at the electrochemically active sites. However, dominant micropores and small mesopores (2-4 nm) of these ZIF-derived M-N-C catalysts have significantly limited access to reactants. Such restriction in local transport can limit the formation of effective TPBs, leading to underutilization of the active sites in the current ZIF-derived M-N-C catalysts.[22-24] Therefore, merely increasing the concentration of active sites in catalysts is not effective in enhancing the MEA performance. Macroporosity is limited in ZIF-derived M-N-C catalyst in electrodes and only can be created between the carbon particle agglomerates (up to 20-30 μm) due to the stacking of primary carbon particles (50-100 nm).[25] The lack of large connected pores leads to the poor dispersion of the ionomer into the interior of primary catalyst particles and thus results in lower ionic conductivity within electrodes.[26-28] Therefore, advancements in MEA performance

require innovative electrode design with tailored micro-, meso- and macroporosity, aiming at maximizing the density of effective TPBs and improving mass and charge transport.[29-33]

Electrospinning has proven a practical approach to introducing large meso- and macropores in nanomaterials. [15, 34-47] The carbon nanofiber (CNF) morphology obtained from this process is the key to ensuring high macroporosity in catalytic layers. Hence, we hypothesized that co-electrospinning ZIFs precursors with selected carrying polymers followed by thermal activation could produce CNFs with increasing distribution of macroporous carbon structures to mitigate particle agglomeration, while also maintaining sufficient microporosity in each nanofiber for hosting MN_4 active sites.

The insufficient stability and durability of M-N-C catalysts remain another technical barrier preventing their uses in viable applications.[30, 48] Of the several competing degradation mechanisms, metal demetallation and carbon corrosion are two critical reasons for the rapid performance decay of M-N-C catalysts. Although Fe-N-C catalysts possess the highest activity of the transition metal catalysts, Fe ions are known to catalyze the formation of hydroperoxyl radical oxygen species (ROS) *via* the Fenton reactions when they meet H_2O_2, an unwanted byproduct of the ORR process.[49, 50] The as-generated ROS further destroys the local carbon structure and MN_4 sites in the catalysts. Even worse, it attacks the ionomer and membrane in PEMFCs, thereby causing severe failure of MEAs. Thus, the development of Fe-free M-N-C catalysts has attracted increasing attention to mitigate the Fenton reactions (*e.g.*, via such as Co and Mn).[6, 10, 15, 49] Carbon corrosion is also detrimental to catalyst stability by destroying MN_4 active sites and reducing electrode conductivity.[51, 52] It also leads to the collapse of the TPBs and water flooding in the cathode, resulting in severe proton and bulk gas transport resistance.[8] The M-N-C catalysts derived from ZIF-8s generally have a lower degree of graphitization due to the use of limited metal doping and lower peak pyrolysis temperature, which primarily provides abundant defects and N dopants to accommodate high-density single metal sites, but with lower corrosion resistance.[53, 54] Thus, the stability issues associated with carbon corrosion become more severe for these M-N-C catalysts.

Simply introducing highly graphitized carbon materials, such as carbon nanotubes and carbon fibers, may pay the penalty at the expense of losing defects for anchoring MN_4 sites owing to their relatively low surface area and insufficient porosity.[51, 55] Thus, it is critical to balance active site density and the degree of graphitization in catalysts to achieve considerably enhanced durability without compromising activity.[56, 57] The carbonized fibers through electrospinning active metal-doped ZIF-8 may contain sufficient MN_4 sites in catalysts, which can enhance carbon corrosion resistance and retain activity.

In this work, using the electrospinning technique, we prepared an innovative 3D fibrous catalyst architecture to maximize the utilization of single-atom cobalt sites for high-performance M-N-C cathodes. It consisted of interconnected porous carbon nanofiber networks with hierarchical structures, which was generated through electrospinning Co-doped ZIFs and selected dual carrying polymers followed by two-step thermal treatments. The two-step strategy is very critical. The first step at a relatively low temperature is to create porosity, and the second step at a higher temperature can generate active CoN_4 sites. The new catalyst contained atomically dispersed CoN_4 sites and Co nanoparticles enclosed by carbon shells. The enhanced intrinsic activity of CoN_4 sites is due to the dominantly surrounding graphitic N dopants. Importantly, it exhibited dramatically enhanced stability and durability in both aqueous electrolytes and MEAs. We employed the unique nanoscale X-ray computed tomography (nano-CT) imaging to verify that the electrospun Co-N-C catalyst led to uniform ionomer distribution without large aggregates. Therefore, the hierarchically porous carbon features in the catalyst significantly promote the electrode performances in MEAs through exposing more accessible active sites, realizing uniform ionomer coverage around catalysts, and facilitating mass/proton/electron transport.

2. Results and Discussion

2.1 Synthesis, morphology and pore structure

Figure 1a depicts the basic principles and procedures to prepare the Co-N-C catalyst through the electrospinning approach, which contains nitrogen coordinated single Co sites in carbon fibers with hierarchically porous structures. The porous carbon nanofiber (PCNF)-based Co catalyst is labeled as Co-N-PCNFs. The Supporting Information provides detailed synthetic procedures. In brief, chemically Co-doped ZIF-8 (Zn/Co-ZIFs) nanocrystals were firstly incorporated into selected dual polyacrylonitrile (PAN) and polyvinylpyrrolidone (PVP) polymers. Precursors were electrospun from this mixture into fibers with a length of hundreds of microns, which is labeled as Zn/Co-ZIFs/PAN/PVP for subsequent thermal activation. As a comparison, the PAN/PVP nanofibers were electrospun without containing Zn/Co-ZIF nanocrystals (**Figure S1a-c**) and had smooth surfaces and an average fiber diameter of around 500 nm. In contrast, the surfaces of the Zn/Co-ZIFs/PAN/PVP nanofiber precursor appeared rough (**Figure 1b** and **Figure S1d-f**), implying embedding Zn/Co-ZIFs nanoparticles uniformly into the polymeric nanofibers, while maintaining the original fibrous architecture. These nanofibers constructed a unique 3D network structure. Afterward, a two-step thermal treatment in an inert atmosphere was applied through a heating treatment at 900 °C for two hours, followed by a second thermal treatment at 1100 °C for two hours. The rationale of the design is that the first pyrolysis process partially graphitizes ZIF-8 and PAN to form carbon fibers. At this stage, the decomposition of PVP domains could create large mesopores in each fiber. Also, the evaporation of Zn from ZIF-8 precursors can generate sufficient micropore and carbon defects. The second thermal activation at 1100 ºC yields the active CoN_4 sites embedded in carbon fiber supports (**Figure S2-S7**). Besides, the second pyrolysis would lead to an inevitable loss of micropores and a specific surface area. However, large pores with a diameter > 200 nm seem to be more apparent in the nanofibers of the Co-N-PCNF catalyst. A higher graphitization degree and an increased graphitic N content were generated in the Co-N-PCNF catalyst (**Figure S5-S6**). The

fibrous network structures were retained after the thermal treatments but led to a reduction of fiber lengths from hundreds of microns to around 4 μm (**Figure 1c** and **Figure S4**). This change is likely due to the decomposition of PVP. As the solvent was evaporated during the fiber formation process, PVP and PAN were expected to have a phase separation.[58] According to the thermogravimetric analysis (TGA) of PVP and PAN during the carbonization (**Figure S8**), PAN formed a carbon backbone owing to a higher carbon yield. In contrast, PVP acted as the sacrificial polymer and the pore-forming agent as well as an additional nitrogen source to provide more N sites for the stabilization of isolated cobalt sites. As a result, more PVP in the PAN/PVP polymer phase, more portions of PAN/PVP polymers were decomposed and burned away during the pyrolysis. As evidenced in **Figure S9**, increasing the PVP content resulted in shorter fiber segments. Excess PVP content caused the collapse of the fibrous morphology. The ratio of Zn to Co in ZIF precursors plays a similar role in affecting the morphology of carbon nanofibers in catalysts. Because of the relatively low boiling point of zinc at 907 °C, Zn evaporation from ZIF precursors during the first-step pyrolysis generated a hollow structure in the nanofibers. Excess Co dopants led to the agglomeration of single metal sites to form metallic Co particles, which further catalyze carbon fibers with a higher degree of graphitization and cause the destruction of carbon structure (**Figure S10**). As a result, the optimal ratios of PVP to PAN and Co to Zn in ZIF-8 precursors yields a Co-N-PCNF catalyst with a desirable interconnected 3D porous network (**Figure 1d-1e** and **Figure S11**), compared to the traditional particle-like Co-N-C catalysts (**Figure S12**).[10] For comparison, a catalyst was synthesized through mixing a particle-like Co-N-C carbonized from Zn/Co-ZIF-8 with dual carrying polymers for the electrospinning followed by thermal treatment at 1100 °C (labeled as Co-N-C@CNF). Since the pre-treated carbon does not undergo significant morphology change during the thermal treatment, solid particle morphology was apparent in each nanofiber (**Figure S13**). Therefore, direct use of Zn/Co-ZIF precursors, rather than a Zn/Co-ZIFs-derived carbon, is vital to achieving the unique porous structure. Overall, the innovative use of auxiliary polymer PVP and the adjustment of Co content

in the ZIFs precursor is crucial for constructing the interconnected porous morphology in the Co-N-PCNF catalyst.

Comprehensive characterization was employed to explore the physical structures (*i.e.*, bulk carbon structure, pore size distribution, and specific surface area) of the Co-N-PCNF catalyst. In particular, these high-angle annular dark field-scanning transmission electron microscope (HAADF-STEM) images (**Figure 2a-2d** and **Figure S14)** reveal that the connected networks constructed large meso- and macroporous structures inside each fiber in the Co-N-PCNF catalyst. Compared to other nanofiber catalysts,[30, 35, 36, 39-41, 45] the porous fiber structure with the interconnected channel size around 200 nm (**Figure S4**), along with the 3D network architecture, is unique for the Co-N-PCNF catalyst. The textural porosity of a particle-like Co-N-C and the Co-N-PCNF catalyst was determined by using N_2 adsorption-desorption isotherms. The Co-N-C sample exhibited the typical type I isotherm (**Figure 2e**) associated with its dominant microporous characteristics. Pores in the Co-N-C sample are often in the range of 1 to 2 nm (**Figure 2f** and **Table S2**). It is essential to clarify that only the micropore-hosted CoN_4 moieties near the external surface of catalysts can participate in the ORR. In contrast, those buried in the dense carbon matrix stay inactive (**Figure S15**).[30, 59] The small particle size (less than 200 nm) for the Co-N-C also led to ultra-densely packed, large resistance for flow, and discontinuous network for electron transfer (**Figure S16-S17**).

In contrast, the Co-N-PCNF catalyst possessed multimodal pore size distribution with interconnected micro-, meso-, and macropores. The sufficient micropores in each nanofiber derived from ZIF-8s were essential for hosting atomic CoN_4 active sites. A remarkable hysteresis loop of type IV isotherm is indicative of dominant mesopores in the Co-N-PCNF catalyst. Besides, the macropores (ca. 200 nm) in the individual fibers guided the reactants to active cites, and the secondary macropores between entwined fiber backbones at micron level allowed abundant gas flows to diffuse in catalyst layers due to much lower pressure drop and formed a freeway network for electron transfer (**Figure S18**). Unlike the

dominant amorphous carbon structure in traditional Co-N-C catalysts directly from ZIF-8 precursors, distinct graphitic carbon layers were apparent in the Co-N-PCNF catalyst (**Figure 2g-h** and **Figure S19**). Two sharp peaks assigned to the (002) and (101) basal planes in the X-ray diffraction (XRD) pattern indicate the presence of a large number of graphitic carbon domains in the Co-N-PCNF catalyst (**Figure 2i**). The increased degree of graphitization for the Co-N-PCNF catalyst sample was further analyzed in the Raman spectra (**Figure 2j**). The peaks at about 1337 and 1587 cm^{-1} are designated as the D and G bands of the graphite structure, respectively. The I_D/I_G ratio value in the Co-N-PCNF was much lower than that in the Co-N-C (0.78 *vs.* 0.88), suggesting a relatively higher graphitic structure. The sharp peaks appearing in the 2500-3500 cm^{-1} region also indicate the ordering carbon structures in the Co-N-PCNF catalyst. The use of dual polymers (*i.e.*, PVP and PAN) and the optimal Zn/Co ratios have a profound influence on the degree of graphitization of Co-N-PCNF samples. As discussed above, due to the lower carbon yield of the PVP domain, PAN induced the graphitic carbon and graphitic N dopants. An appropriate amount of PVP generated highly graphitized carbon (**Figure S20**) while maintaining fibrous morphology. Increasing the Co dopants led to the agglomeration of single metal sites to form Co metal particles during high-temperature pyrolysis (**Figure S10**), which are widely considered to promote higher graphitization degree of carbon matrix (**Figure S21**). The increased graphitization degree of the Co-N-PCNF catalyst is also corroborated by the increased intensity of π-π* satellite in X-ray photoelectron spectroscopy (XPS) C 1s peak (**Figure S22** and **Table S3**). The highly graphitized carbon matrix is beneficial for enhancing carbon corrosion resistance, thereby dramatically promoting catalyst stability (**Figure S23**). Similar to traditional Co-N-C catalysts, there are multiple N dopants in the catalyst, including pyridinic N (398.5 eV), graphitic N (401.2 eV), oxidized N (403.5 eV), and N coordinated with single atomic Co sites (denoted as Co-N) (399.5 eV) (**Figure 2k-2l**). However, the Co-N-PCNF catalyst contained a relatively higher ratio of graphitic N over pyridinic N when compared to traditional Co-N-C catalysts (**Table S4**). The increased graphitic N content is likely due to the use of PAN. It is consistent

with the increment of the graphitization degree in the Co-N-PCNF catalyst. This co-electrospinning Co-doped ZIFs with well-selected dual carrying polymers presents great promise to achieve a desirable hierarchical porous structure with increased graphitization in Co-N-C catalysts for PGM-free electrodes.

2.2 Single Co site structure and coordination

XRD did not detect any crystalline Co species in the catalyst (**Figure 2i**). Meanwhile, the scanning transmission electron microscopy with energy-dispersive X-ray spectroscopy (STEM-EDS) (**Figure 3a-d** and **Figure S24)** elemental maps suggest a homogeneous distribution of doped Co and N in the Co-N-PCNF catalyst (**Figure 25**). Subsequently, aberration-corrected HAADF-STEM imaging with electron energy loss spectroscopy (EELS) was used to observe the atomically dispersed single Co site and co-existed with N at the atomic level (**Figure 3e-3g** and **Figure S26-S27**). Point spectra acquired with the electron beam placed on the bright atoms (*i.e.*, blue circle in **Figure 3g**) revealed both N and Co signals, which strongly suggests coordination. Nanoclusters consisting of a few metal atoms were occasionally observed as well. Co-N coordination and chemical information were further examined by using X-ray absorption spectroscopy (XAS).[10, 60] **Figure 3h** is the Co K-edge X-ray absorption near edge structure (XANES). The result reveals that the Co-N-PCNF catalyst has a slightly higher oxidation state compared to Co foil, suggesting that the Co species in the catalyst were mixed with oxidized Co and Co metallic nanoparticles, and also explaining that the lack of XRD signal of Co nanoparticles could be ascribed to the amorphous nature. The extended X-ray absorption fine structure (EXAFS) analysis further indicates that both metallic Co-Co and Co-N scattering paths were found in Fourier-transformed EXAFS (**Figure 3i-3j**). A linear combination fit using Co-N_4 structure from CoPc, and metallic Co from Co foil was performed to quantify the species of Co in the catalyst (**Figure S28**). The fitting result indicates that the catalyst contains 61.3% Co-Co and 38.7% Co-N_4. Furthermore, the model-based EXAFS indicates the coordination number (CNs) for Co-N and Co-Co in the Co-N-PCNF catalyst was 1.2 and 6.7, respectively (**Table S7-S10**). Since the XAS measurement is an ensemble average,[61] actual N

coordination can be scaled up using their percentage ratio to be 3.2±1.0 and 10.9±0.6 for Co-N and Co-Co, respectively. These metallic nanoparticles are enclosed by a few carbon layers (**Figure S29**) and are responsible for the formation of graphitized carbon in the catalyst but at the expense of losing defects for anchoring additional single Co metal sites. Considering that XAS measurement is sensitive to the existence of nanoparticles, the density of Co sites in the Co-N-C and Co-N-PCNF was further determined by using the XPS analysis (**Table S5**) and Co 2p analysis (**Table S6** and **Figure S30-S31**). The results suggest that the density of Co sites in the catalyst surface layers of the Co-N-PCNF catalyst was comparable to our previous atomically dispersed single Co site catalysts[10] (0.4 *vs*. 0.3 *at.* %). Thus, although the co-existence of Co nanoparticles, the atomically dispersed CoN_4 active sites are in the Co-N-PCNFs catalyst to catalyze the ORR. The fiber-like Co-N-PCNF contains less zinc (0.1 *at*. %) when compared to traditional particle-like Co-N-C (zinc: 0.4 *at*. %). The reduced Zn content is an advantage to provide more defects to host active Co sites and minimize the possible contaminations to membranes and ionomer in cathodes. Thus, the electrospun Co-N-PCNF catalyst provides an ideal balance between highly graphitized carbon matrix and sufficient atomically dispersed CoN_4 sites and graphitic N dopant, along with favorable porosity for increasing the utilization active sites and facilitating mass transport.

2.3 Oxygen Reduction Activity and Stability in Acids

We evaluated ORR activities of a variety of relevant samples by using steady-state staircase voltammetry (SCV) measurement in 0.5 M H_2SO_4 solution. Although the second thermal treatment does not change overall morphology obviously, it effectively improved ORR activity of the electrospun Co-N-PCNF catalyst, exhibiting a larger electrochemically accessible surface areas (EASA), a higher onset potential (E_{onset}), and a positive half-wave potential ($E_{1/2}$) shift of 40 mV relative to the sample processed with one-step pyrolysis (**Figure S32-S34**). This remarkable activity improvement was primarily attributed to the formation of active CoN_4 sites after the second thermal treatment at 1100 °C. In our previous work,[10] we carefully studied the temperature dependence on ORR activity. The Co-N-C catalyst treated from 900

°C exhibited low activity, while increased heating temperature up to 1100 °C yielded dramatically enhanced ORR activity, suggesting the formation of active CoN_4 sites, rather than moderate metal-free N dopants. However, high heating temperature led to a slight reduction in Co and total N content (0.1 *at.* % in Co and 0.3 *at.* % in total N) in the Co-N-PCNFs **(Table S5)**. Further optimizations of PVP/PAN ratios and Nafion contents in ink (**Figure S35-S36**) achieved the best performing Co-N-PCNF catalyst. It exhibited encouraging ORR catalytic activity in acids (E_{onset} = 0.95 V_{RHE} and $E_{1/2}$ = 0.81 V_{RHE} at a loading of 0.6 mg/cm^2, 900 rpm in 0.5 M H_2SO_4) (**Figure 4a**). The H_2O_2 yield was also measured by using a rotation ring-disk electrode (RRDE) to determine the four-electron selectivity during the ORR (**Figure 4b**). The Co-N-PCNF catalyst showed a relatively higher H_2O_2 yield (ca. 9%) corresponding to an electron-transfer number of ca. 3.8 during ORR, probably due to the existence of Co metal clusters.[62] Since the Fenton reaction for Co ions is less thermodynamically favorable over Fe ions (**Equations S1-S3**), the atomically dispersed Co sites embedded in highly graphitized carbon fibers are stable during the ORR in acidic media. The effect of Co doping content on ORR activity followed a "volcano plot" trend (**Figure 4c and S37**). The sample without Co doping presented the lowest catalytic activity. The activity was continuously increased as Co doping increased up to 30 at. % and then decreased with higher Co doping. This observation confirmed the significant role of CoN_4 active sites in promoting ORR activity. Lower doping produces insufficient active site, but higher doping results in Co agglomeration and unfavorable carbon structures (*i.e.*, fewer defects and porosities).

A higher degree of graphitization in the Co-N-PCNF catalyst enables improved stability in acids, as evidenced by extensive accelerated stability tests (ASTs). Long-term durability tests were conducted by holding at a constant potential of 0.85 V_{RHE} for 50 hours in O_2 saturated 0.5 M H_2SO_4. The Co-N-PCNF catalyst conveyed excellent stability in terms of insignificant loss of $E_{1/2}$ and 87% retention of its initial current density under such a harsh condition (**Figure 4d** and **S38**). Under identical conditions, the traditional Co-N-C catalyst exhibited a loss of $E_{1/2}$ up to 35 mV and only retained 83% of its activity

(**Figure 4e** and **Figure S39-S40**). During the stability test, we performed voltage cycling for hundreds of cycles before recording their steady-state ORR polarization plots. We found that apparent performance recovery in the Co-N-PCNFs catalyst occurred, likely due to the removal of weakly adsorbed functional groups at the catalyst surface. It might be related to the surface carbon oxidation of the catalyst. However, the Co-N-C catalyst suffered from significant irreversible degradation, especially in the first 10 hours. The potentiostatic test also confirmed the enhanced durability of the Co-N-PCNF catalyst at a relatively low, but more practical potential 0.7 V_{RHE} (**Figure 4f** and **S41**). Likewise, during the potential cycling AST (from 0.6 to 1.0 V_{RHE} in O_2-saturated 0.5 M H_2SO_4 solution), the Co-N-PCNF catalyst exhibited negligible degradation of ORR activity after 30,000 AST potential cycles (**Figure 4g**), due to the strong M-N bonding and robust carbon structure. The degradation of previously reported Co-N-C catalysts is likely caused by the dementallation of Co from CoN_4 coordination and the oxidation/corrosion of local carbon around CoN_4 sites. As for the traditional atomically dispersed and nitrogen coordinated CoN_4 sites with particle morphologies (traditional Co-N-C) developed by our group, we have carefully studied the catalyst after potential cycling to determine the possible changes in morphologies and local atomic structures.[10] HADDF-STEM images indicated that the 3D carbon architecture was retained, suggesting the stability of carbon in the catalyst. The atomically dispersed Co sites were apparent and incorporated at the edge of carbon planes. The co-existence of Co and N at the atomic level was verified by using the EELS after the stability tests. In this work, the electrospun Co-N-C catalyst demonstrated even better stability when compared to the previous one (less 5 mV *vs.* 30 mV), as shown in **Figure 4i**. We recorded CVs for the Co-N-PCNF catalyst before and after different stability tests, which can characterize the change of the carbon surface. (**Figure S42**). Regardless of the testing protocols, the insignificant change of carbon surface indicated the excellent tolerance of carbon corrosion for the electrospun Co-N-PCNF catalyst. Therefore, due to the dramatically enhanced stability relative to the traditional

Co-N-C catalyst, we believe that the Co-N coordination and carbon structures in the electrospun Co-N-PCNF catalyst likely retains intact.

The corrosion resistance of carbon in catalysts was further assessed by cycling at a high potential range (from 1.0 to 1.5 V_{RHE}) in N_2-saturated 0.5 M H_2SO_4. After 20,000 cycles, the degradation of the Co-N-PCNF catalyst was only 20 mV $E_{1/2}$ loss (**Figure 4h-i** and **Figure S43a**), much less than the loss (50 mV in $E_{1/2}$) measured in the Co-N-C catalyst. Because of the minimal degradation (12 mV in $E_{1/2}$) of the PCNFs (fiber catalyst without Co-doped ZIF) (**Figure S43b**), a higher degree of graphitization in the Co-N-PCNFs catalyst can dramatically enhance the carbon corrosion resistance, thus promoting the stability of catalysts.

2.4 Synergy of graphitic N Dopants and CoN_4 Site for enhanced activity

We performed the DFT calculations to elucidate the intrinsic activity enhancement of the Co-N-PCNF catalyst (**Figure 5**). According to our XPS results of showing increased graphitic N, we construct several models, in which a CoN_4 site is embedded in a graphene layer containing 0 to 4 extra graphitic N dopants. The CoN_4 model is similar to the one in our previous studies.[15, 63, 64] The possible graphitic N doping sites in our simulation cell with periodic boundaries are marked in **Figure S44**. Here, we performed DFT energy calculations on a total of 24 possible configurations of the catalyst models (**Figure S45-S48**) to identify the most energetically favorable CoN_4-N_x (x=1 to 4) configurations. Our results indicate that the formation of N-N pair neighboring to the CoN_4 moiety was largely unfavored (**Table S11)**, which is in contrast with a previous study on the Fe-N-C catalyst.[51] The lowest-energy configurations of CoN_4-N_1, CoN_4-N_2, CoN_4-N_3, and CoN_4-N_4 are shown in **Figure 5a**.

The extra doping of graphitic N atoms was predicted to cause a considerable change in the electron charge of adjacent C atoms. In a comparison of charge distribution between the structures with and without extra graphitic N dopants (**Figure 5b**), pronounced charge accumulation is on the C atoms adjacent to additional N dopants in all CoN_4-N_x (x=1 to 4) structures. Such electronic change on the C

atoms due to graphitic N doping significantly affects the O=O bond cleavage process during the ORR on the CoN_4 active site. **Figure 5c** shows the O=O bond cleavage pathway on CoN_4 and CoN_4-N_4 structures. For the ORR on all CoN_4-N_x (x=1 to 4), *OH after O=O bond cleavage from *OOH is preferable to adsorb on the C atom between two N dopants. The activation energy for *OOH dissociation with extra graphitic N dopants is dramatically lowered as compared to that of the CoN_4 with no surrounding graphitic N dopants (**Figure 5d**). For example, with one or two additional graphitic N dopants around CoN_4 active site, the activation energy was lowered by ~0.3 eV from 1.15 eV on the pristine CoN_4 site. Moreover, the predicted free energy evolution shown in **Figure S49** suggests that the ORR is thermodynamically feasible on this CoN_4-N_x (x=1 to 4) sites with thermodynamic limiting potentials close to that on the CoN_4 site without extra N dopants. Therefore, our DFT calculations predict that additional graphitic N dopants around a CoN_4 moiety can enhance its activity for the ORR because these N dopants increase the charge of adjacent C atoms and thus lower the activation energy for the *OOH dissociation step of ORR. Therefore, generating more graphitic N dopants is one of the advantages of enhancing the intrinsic activity of the Co-N-PCNF catalyst.

2.5 MEA Performance and Durability

The Co-N-PCNF catalyst, featured with unique hierarchical fiber network architectures, was further evaluated in MEAs. Under 1.0 bar H_2-O_2 condition, the Co-N-PCNF cathode achieved an open-circuit voltage (OCV) of 0.95 V and a peak power density of 0.71 W cm^{-2} (**Figure 6a**). These performance metrics exceed those of the traditional Co-N-C catalyst (0.88 V and 0.50 W cm^{-2}, respectively). The Co-N-PCNF catalyst achieved an encouraging current density of 15 mA cm^{-2} at 0.9 $V_{iR\text{-}free}$ (**Figure S50**), which is higher than those measured with traditional Co-N-C catalysts (1.6 and 3.0 mA/cm^2).[10, 15] The experimental result further verified that graphitized N dopants could substantially improve the intrinsic ORR activity of CoN_4 active sites in kinetic ranges. The Co-N-PCNFs cathode was subsequently evaluated under practical H_2/air conditions (1.0 bar) to understand the mass-transport properties better

(**Figure 6b**). The MEA with the Co-N-PCNF cathode outperformed the comparative Co-N-C catalyst throughout the entire voltages region in an H_2-air cell. The OCV was 0.93 V for the Co-N-PCNF cathode, much higher than that of the Co-N-C cathode (0.84 V). The Co-N-PCNF-based MEA reached a current density of 46 mA cm^{-2} at 0.8 V and 185 mA cm^{-2} at 0.7 V, representing an order of magnitude improvement compared with the conventional Co-N-C-based MEA (5 mA cm^{-2}). The maximum power density (P_{max}) of Co-N-PCNF cathode reached a remarkable value of 0.40 W cm^{-2} *vs.* that of the Co-N-C cathode (0.23 W cm^{-2}). The P_{max} can further increase to 0.45 W cm^{-2} under higher pressure (2.0 bar air), but the increment is marginal, suggesting facial O_2 transport already at low pressure (**Figure S51**). The encouraging power density endowed by the Co-N-PCNF cathode represents a record-high activity measured in MEAs by using Fe-free and PGM-free cathodes (**Figure 6c**) and comparable to state-of-the-art Fe-N-C catalysts (**Table S1**). With the same loading, the Co-N-PCNF cathode indeed possessed a thicker cathode catalyst layer when compared to the traditional Co-N-C cathode, suggesting a more porous electrode structure. The particle-like Co-N-C catalyst (200 nm) led to ultra-densely packed, large resistance for flow, and discontinuous network for electron transfer. The macropores (ca. 200 nm) in the individual fibers of the Co-N-PCNFs catalyst facilitate the diffusion of the reactants to active cites. The secondary macropores between entwined fiber backbones at the micron level allowed abundant gas flows to diffuse in catalyst layers due to much lower pressure drop and formed a freeway network for electron transfer. Besides, a highly graphitized carbon matrix in the Co-N-PCNF catalyst was beneficial for improving facile electron conductivity. Thus, the high utilization of active sites and efficient mass transport in the Co-N-PCNF cathode can promote the outstanding MEA performance, which is offered by the distinct porous fibrous morphology and well-designed hierarchical porous structure. The current work is a preliminary exploration. Controlling the thickness of the cathode catalyst layer are highly desirable by exploring optimal loading, I/C ratios, and hot press conditions, etc., which provide significant room to further improve MEA performance.

MEA durability of the Co-N-PCNF cathode was evaluated by using multiple stability testing protocols, including voltage cycling AST and potentiostat tests in H_2/air cells. **Figure 6d** recorded the polarization curves measured intermittently under repeated cell voltage sweeps from 0.6 to 0.95 V, aiming to study possible activity loss. The drop of the fuel cell voltage at a current density of 0.8 A cm^{-2} after 20,000 cycles was only 8 mV, well within the DOE target of < 30 mV loss.[65, 66] For the first time, the PGM-free cathode demonstrated such encouraging durability under practical H_2/air conditions. The durability of the MEA was also performed at a constant cell voltage of 0.7 V in an H_2-air cell. Similar to previously reported M-N-C cathodes, the rapid initial decay occurred during the first 5 hours (**Figure S52**). However, the overall drop in current density observed in the Co-N-PCNFs cathode is lower than those of the traditional Co-N-C catalyst (**Figure S53-S54)** and other M-N-C catalysts (**Table S12**). I-V polarization and power density plots of the MEA under H_2-air conditions were recorded during the potentiostat test (**Figure 6e**). Before recording the I-V polarization plots under H_2/air, we performed voltage cycling in H_2/N_2 conditions to re-active the cathode. We found apparent performance recovery after the H_2/N_2 cycling (**Figure 6e**), likely due to the removal of weakly adsorbed functional groups at the catalyst surface. The reversible performance loss might be related to the surface carbon oxidation of the catalyst. These results are consistent with the observation in aqueous solution for RDE tests. This is the reason why polarization plots exhibit less degradation (**Figure 6f**) when compared to the tests by using continuous chronoamperometry at 0.7 V. The Co-N-PCNF cathode possessed significantly enhanced stability when compared to reported M-N-C cathodes (**Table S12**). For example, in the kinetic region of an H_2/air cell, the current density at 0.7 V was only decreased from 185 mA cm^{-2} to 163 mA cm^{-2} after 22-hour tests (**Figure 6f**), and the current density loss at 0.8 V was only 10 mA cm^{-2} after the stability test. The Co-N-PCNFs cathode was also featured with an excellent mass-transport property because of negligible degradation of current density at 0.4 V in after the stability test *vs.* the significant degradation observed in other M-N-C catalysts (**Table S12**). According to our prior work[8], the

degradation is dependent on testing protocols. For example, voltage/potential cycling often leads to a less significant loss. Oppositely, at a constant high voltage/potential above 0.7 V, the degradation may be due to the severe carbon corrosion and the associated loss of MN_4 sites, which are caused by H_2O_2. The confined H_2O_2 formation within the cathode could be more harmful than in an aqueous electrolyte. Therefore, the Co-N-PCNFs still suffered from a noticeable decay of current density during the challenging stability test at 0.7 V, when compared to voltage cycling from 0.6 to 0.95 V in H_2/air MEAs. The MEA performance was still not sufficient to reach automotive performance targets with PGM-free cathodes (*e.g.*, power density (1.0 W/cm^2) and lifetime (5,000 h) at the automotive rated cell voltages for suitable Q/ΔT (~ 0.7 V)). However, for the first time, we demonstrated promising MEA durability for PGM-free cathodes. The significantly improved stability and durability of the Co-N-PCNF cathode in MEAs stem from the following reasons. First, increased graphitization degree, yet exposing more active sites, can benefit corrosion resistance of the carbon matrix. Second, the unique porous nanofiber morphology maintains structural integrity for efficient mass transport and charge transfer. Finally, robust TPBs during the ORR is maintained due to the optimal pore size distribution between interconnected micro-, meso-, and macropores in favor of timely water removal.

2.6 Ionomer and catalysts interface studies by using nano-CT imaging

Our prior work has shown that 3D electrode structures (*e.g.*, pore size, pore distribution, and catalyst geometry) and ionomer distribution strongly affected the PGM-free cathodes in MEAs.[25, 26] We further evaluated these macroscopic properties for the promising Co-N-PCNFs cathode by using nano-CT imaging (with a resolution of about 50 nm). As developed by Komini Babu *et al.*,[26] the nano-CT allows us to characterize the overall ionomer distribution by using the Cs^+ signal in absorption contrast and the pore/solid morphology through Zernike phase contrast. **Figures 7a** and **7b** show the 3D ionomer distributions in virtual slices and volume renderings, respectively. We observed that the ionomer imaging shows good surface coverage of the fibrous carbon network, contributing to the high MEA performance.

The ionomer map does not show any thick ionomer films or large (> 1 μm) ionomer agglomerates. The coverage over the fibers at any particular depth is uniform, especially compared to aggregates in our past work and imaging of CM-PANI-Fe electrodes.[67] However, there is an apparent gradient in ionomer content from the membrane side to the gas diffusion layer (GDL) side of the cathode. This observation is quantitatively illustrated in **Figure 7c**, where the average intensity of the absorption in-plane slices are plotted through the thickness of the cathode. This result may be due to the additional ionomer infiltration after the ionomer overcoat applied to the cathode following the GDL coating. The purpose is to reduce the contact resistance between the cathode and the membrane, as mentioned as "graded-ionomer" concept as demonstraded in **Figure S55**. The Zernike phase contrast dataset was processed, yielding the slice and volume renderings displayed in **Figures 7d** and **7e**, respectively. The intensity data in these figures correspond to the solid carbon/void structure of the porous Co-N-PCNF cathode. For instance, in **Figure 7d**, the Co-N-PCNF cathode structure was homogeneous within the large field of view. It contained no large-scale agglomerates, cracks, or other common large-scale heterogeneities often found with M-N-C cathodes due to the large carbon aggregates.[25, 26] Instead, the structure is consistent with the diameter of the fibers. The macroscale void distribution was quantitatively evaluated using the PoreSpy toolkit.[68] **Figure 7f** depicts the void size distribution, suggesting the lack of voids or cracks larger than 1 μm. A vast majority of the macroporosity resulting from voids has a peak in the distribution at approximately 400 nm, keeping consistent with the fiber diameter. The unique nano-CT imaging highlights a key advantage of the electrospun Co-N-PCNF catalyst, which can eliminate large scale aggregates and yield a well-controlled secondary pore distribution around the catalyst particles, thus facilitating a well-distributed ionomer coverage that does not rely on ionomer infiltration into large aggregates.

3. Conclusion

In summary, we designed an innovative electrode structure in atomically dispersed Co-N-C catalysts

through co-electrospinning procedure of Co-doped ZIF-8s crystals and dual PAN/PVP polymers. Through systematically studied porosity and morphology controls, we emphasized that the polymer selection, metal combination, and thermal treatment are very critical for Co-N-C catalysts, which require a delicate design for advanced electrode structure in practical fuel cell application. The unique interconnected porous fibrous morphology and hierarchical structures were proven effective in promoting the translation of their high intrinsic activity into device-level MEA performance with significantly enhanced stability and durability. DFT calculations elucidated that the dominant graphitic N dopants promote the intrinsic ORR activity of the CoN_4 sites through inducing higher charge density on adjacent C atoms and thus lowering the activation energy for the *OOH dissociation step during the ORR. The Co-N-PCNF catalyst possessed a distinct interconnected porous nanofiber network coupled with multimodal pore size distribution, capable of increasing the utilization of single-atom cobalt sites and maximizing the density of effective TPBs. The abundant ZIFs-derived micropores in each nanofiber were essential for hosting single atomic CoN_4 active sites and thus achieving high catalytic activity. Sufficient mesopores and macroporous voids within and between the fiber network facilitated the mass transfer of reactants (O_2 and H^+) and product (H_2O). As a result, the uniform distribution of ionomer in thick PGM-free cathode layers is mainly responsible for the significantly improved MEA performance, which was verified by using the unique nano-CT imaging.

The electrospun Co-N-PCNF catalyst set a new benchmark of stability and durability for PGM-free catalysts towards ORR in both challenging acidic media and the practical MEA operation conditions under H_2/air cell conditions. The significant enhancement of stability and durability was associated with the higher graphitization degree and enhanced corrosion resistance of carbon structures in the catalyst. The new concepts, approaches, and understanding gained from this work can guide future catalyst design and synthesis to achieve significant advancements in PGM-free cathode MEA performance for PEMFC applications.

Conflicts of interest

There are no conflicts to declare.

Acknowledgment

G. Wu, G. F. Wang, and S. Litster acknowledge the support from U.S. DOE-EERE Fuel Cell Technologies Office (DE-EE0008076). G. Wu is grateful for the financial support from the National Science Foundation (NSF) (CBET-1604392, 1804326). L. Fei acknowledges the financial support from NSF (No.1832963) and Chevron Corporation for providing Chevron Endowed Professorship in Chemical Engineering at UL Lafayette. Electron microscopy research was conducted at the Center for Functional Nanomaterials at Brookhaven National Laboratory (S. Hwang and D. Su, under contract No. DE-SC0012704) and the Center for Nanophase Materials Sciences of Oak Ridge National Laboratory (D. A. Cullen and K. L. More), which both are DOE Office of Science User Facilities. Z. F. thanks for the startup funding from Oregon State University. X-ray absorption analysis used the resources of the beamline 12-BM of the Advanced Photon Source (APS), a U.S. DOE Office of Science User Facility operated for the DOE Office of Science by Argonne National Laboratory under Contract DE-AC02-06CH11357. G. F. Wang also gratefully acknowledges the computational resources provided by the University of Pittsburgh Center for Research Computing as well as the Extreme Science and Engineering Discovery Environment (XSEDE), which is supported by NSF (ACI-1053575).

References

[1] X. X. Wang, M. T. Swihart, G. Wu, Nat. Catal. 2019, 2, 578.

[2] X. Tian, X. F. Lu, B. Y. Xia, X. W. D. Lou, Joule 2020, 4, 45.

[3] Y. He, Q. Tan, L. Lu, J. Sokolowski, G. Wu, Electrochem. Energy Rev. 2019, 2, 231.

[4] Y. Li, H. Wang, C. Priest, S. Li, P. Xu, G. Wu, Adv. Mater. 2020, 10.1002/adma.202000381, 2000381.

[5] G. Wu, K. L. More, C. M. Johnston, P. Zelenay, Science 2011, 332, 443.

[6] J. Li, M. Chen, D. A. Cullen, S. Hwang, M. Wang, B. Li, K. Liu, S. Karakalos, M. Lucero, H. Zhang, C. Lei, H. Xu, G. E. Sterbinsky, Z. Feng, D. Su, K. L. More, G. Wang, Z. Wang, G. Wu, Nat. Catal. 2018, 1, 935.

[7] Y. He, S. Hwang, D. A. Cullen, M. A. Uddin, L. Langhorst, B. Li, S. Karakalos, A. J. Kropf, E. C. Wegener, J. Sokolowski, M. Chen, D. Myers, D. Su, K. L. More, G. Wang, S. Litster, G. Wu, Energy Environ. Sci. 2019, 12, 250.

[8] H. Zhang, H. T. Chung, D. A. Cullen, S. Wagner, U. I. Kramm, K. L. More, P. Zelenay, G. Wu, Energy Environ. Sci. 2019, 12, 2548.

[9] T. Asset, P. Atanassov, Joule 2019, 4, 33.

[10] X. X. Wang, D. A. Cullen, Y. T. Pan, S. Hwang, M. Wang, Z. Feng, J. Wang, M. H. Engelhard, H. Zhang, Y. He, Y. Shao, D. Su, K. L. More, J. S. Spendelow, G. Wu, Adv. Mater. 2018, 30, 1706758.

[11] H. Zhang, S. Hwang, M. Wang, Z. Feng, S. Karakalos, L. Luo, Z. Qiao, X. Xie, C. Wang, D. Su, Y. Shao, G. Wu, J. Am. Chem. Soc. 2017, 139, 14143.

[12] Y. Zhu, J. Sokolowski, X. Song, Y. He, Y. Mei, G. Wu, Adv. Energy Mater. 2020, 10, 1902844.

[13] G. Wu, A. Santandreu, W. Kellogg, S. Gupta, O. Ogoke, H. Zhang, H.-L. Wang, L. Dai, Nano Energy 2016, 29, 83.

[14] M. Chen, Y. He, J. S. Spendelow, G. Wu, ACS Energy Lett. 2019, 4, 1619.

[15] J. Li, H. Zhang, W. Samarakoon, W. Shan, D. Cullen, S. Karakalos, M. Chen, D. Gu, K. More, G. Wang, Z. Feng, W. Zhenbo, G. Wu, Angew. Chem. Int. Ed. 2019, 58, 18971.

[16] H. Zhang, H. Osgood, X. Xie, Y. Shao, G. Wu, Nano Energy 2017, 31, 331.

[17] Q. Shi, S. Hwang, H. Yang, F. Ismail, D. Su, D. Higgins, G. Wu, Mater. Today 2020.

[18] Y. He, S. Liu, C. Priest, Q. Shi, G. Wu, Chem. Soc. Rev. 2020, 49, 3484.

[19] D. Banham, J. Y. Choi, T. Kishimoto, S. Ye, Adv. Mater. 2019, 31, 1804846.

[20] S. Litster, G. McLean, J. Power Sources 2004, 130, 61.

[21] N. R. Sahraie, U. I. Kramm, J. Steinberg, Y. Zhang, A. Thomas, T. Reier, J.-P. Paraknowitsch, P. Strasser, Nat. Commun. 2015, 6, 1.

[22] D. Malko, A. Kucernak, T. Lopes, Nat. Commun. 2016, 7, 1.

[23] Y. Ye, F. Cai, H. Li, H. Wu, G. Wang, Y. Li, S. Miao, S. Xie, R. Si, J. Wang, X. Bao, Nano Energy 2017, 38, 281.

[24] F. Jaouen, M. Lefèvre, J.-P. Dodelet, M. Cai, J. Phys. Chem. B 2006, 110, 5553.

[25] A. Uddin, L. Dunsmore, H. Zhang, L. Hu, G. Wu, S. Litster, ACS Appl. Mater. Interfaces 2020, 12,

2216.

[26] S. Komini Babu, H. T. Chung, P. Zelenay, S. Litster, ACS Appl. Mater. Interfaces 2016, 8, 32764.

[27] D. Banham, T. Kishimoto, T. Sato, Y. Kobayashi, K. Narizuka, J.-i. Ozaki, Y. Zhou, E. Marquez, K. Bai, S. Ye, J. Power Sources 2017, 344, 39.

[28] K. Artyushkova, M. J. Workman, I. Matanovic, M. J. Dzara, C. Ngo, S. Pylypenko, A. Serov, P. Atanassov, ACS Appl. Energy Mater. 2017, 1, 68.

[29] S. H. Lee, J. Kim, D. Y. Chung, J. M. Yoo, H. S. Lee, M. J. Kim, B. S. Mun, S. G. Kwon, Y.-E. Sung, T. Hyeon, J. Am. Chem. Soc. 2019, 141, 2035.

[30] X. Wan, X. Liu, Y. Li, R. Yu, L. Zheng, W. Yan, H. Wang, M. Xu, J. Shui, Nat. Catal. 2019, 2, 259.

[31] J. Pampel, T.-P. Fellinger, Adv. Energy Mater. 2016, 6, 1502389.

[32] Q. Shi, Y. He, X. Bai, M. Wang, D. A. Cullen, M. Lucero, X. Zhao, K. L. More, H. Zhou, Z. Feng, Y. Liu, G. Wu, Energy Environ. Sci. 2020, doi: 10.1039/D0EE01968B.

[33] S. Liu, M. Wang, X. Yang, Q. Shi, Q. Zhi, M. Lucero, Q. Ma, K. L. More, D. A. Cullen, Z. Feng, G. Wu, Angew. Chem. Int. Ed. 2020, doi:10.1002/anie.202009331.

[34] H. Yang, Q. Lin, Y. Wu, G. Li, Q. Hu, X. Chai, X. Ren, Q. Zhang, J. Liu, C. He, Nano Energy 2020, 70, 104454.

[35] J. Shui, C. Chen, L. Grabstanowicz, D. Zhao, D.-J. Liu, Proc. Natl. Acad. Sci. U.S.A. 2015, 112, 10629.

[36] Q. Cheng, S. Han, K. Mao, C. Chen, L. Yang, Z. Zou, M. Gu, Z. Hu, H. Yang, Nano Energy 2018, 52, 485.

[37] J. Chen, X. Yan, C. Fu, Y. Feng, C. Lin, X. Li, S. Shen, C. Ke, J. Zhang, ACS Appl. Mater. Interfaces 2019, 11, 37779.

[38] M. Rauf, J.-W. Wang, P. Zhang, W. Iqbal, J. Qu, Y. Li, J. Power Sources 2018, 408, 17.

[39] L.-F. Chen, Y. Lu, L. Yu, X. W. D. Lou, Energy Environ. Sci. 2017, 10, 1777.

[40] C. Wang, C. Liu, J. Li, X. Sun, J. Shen, W. Han, L. Wang, Chem. Commun. 2017, 53, 1751.

[41] C. Liu, J. Wang, J. Li, J. Liu, C. Wang, X. Sun, J. Shen, W. Han, L. Wang, J. Mater. Chem. A 2017, 5, 1211.

[42] W. Zhang, X. Yao, S. Zhou, X. Li, L. Li, Z. Yu, L. Gu, Small 2018, 14, 1800423.

[43] C.-L. Zhang, B.-R. Lu, F.-H. Cao, Z.-L. Yu, H.-P. Cong, S.-H. Yu, J. Mater. Chem. A 2018, 6, 12962.

[44] J. Slack, B. Halevi, G. McCool, J. Li, R. Pavlicek, R. Wycisk, S. Mukerjee, P. Pintauro, ChemElectroChem 2018, 5, 1537.

[45] S. Kabir, S. Medina, G. Wang, G. Bender, S. Pylypenko, K. C. Neyerlin, Nano Energy 2020, 104791.

[46] J. Zang, F. Wang, Q.-q. Cheng, X. Liu, L. Ma, C. Chen, L. Yang, Z.-Q. Zou, D. Xie, H. Yang, J. Mater. Chem. A 2020, 8, 3686.

[47] H. Zhang, W. Zhou, T. Chen, B. Y. Guan, Z. Li, X. W. Lou, Energy Environ. Sci. 2018, 11, 1980.

[48] Y. Shao, J. P. Dodelet, G. Wu, P. Zelenay, Adv. Mater. 2019, 31, 1807615.

[49] X. X. Wang, V. Prabhakaran, Y. He, Y. Shao, G. Wu, Adv. Mater. 2019, 31, 1805126.

[50] U. Martinez, S. Komini Babu, E. F. Holby, H. T. Chung, X. Yin, P. Zelenay, Adv. Mater. 2019, 31, 1806545.

[51] D. Xia, X. Yang, L. Xie, Y. Wei, W. Jiang, M. Dou, X. Li, J. Li, L. Gan, F. Kang, Adv. Func. Mater. 2019, 29, 1906174.

[52] T. Ha, J. Cho, J. Park, K. Min, H.-S. Kim, E. Lee, J.-Y. Jyoung, Int. J. hydrogen Energy 2011, 36, 12436.

[53] M. Lefèvre, E. Proietti, F. Jaouen, J.-P. Dodelet, Science 2009, 324, 71.

[54] X. Yan, Y. Jia, X. Yao, Chem. Soc. Rev. 2018, 47, 7628.

[55] X. Fu, N. Li, B. Ren, G. Jiang, Y. Liu, F. M. Hassan, D. Su, J. Zhu, L. Yang, Z. Bai, Adv. Energy Mater. 2019, 9, 1803737.

[56] Z. Qiao, S. Hwang, X. Li, C. Wang, W. Samarakoon, S. Karakalos, D. Li, M. Chen, Y. He, M. Wang, Z. Liu, G. Wang, H. Zhou, Z. Feng, D. Su, J. S. Spendelow, G. Wu, Energy & Environmental Science 2019, 12, 2830.

[57] S. Gupta, S. Zhao, O. Ogoke, Y. Lin, H. Xu, G. Wu, ChemSusChem 2017, 10, 774.

[58] C.-L. Huang, T.-H. Wei, S.-Y. Peng, K.-M. Lee, J. Appl. Poly. Sci. 2019, 136, 48218.

[59] H.-W. Liang, W. Wei, Z.-S. Wu, X. Feng, K. Müllen, J. Am. Chem. Soc. 2013, 135, 16002.

[60] M. Wang, L. Árnadóttir, Z. J. Xu, Z. Feng, Nano-Micro Lett. 2019, 11, 47.

[61] Z. Weng, Y. Wu, M. Wang, J. Jiang, K. Yang, S. Huo, X.-F. Wang, Q. Ma, G. W. Brudvig, V. S. Batista, Nat. Commun. 2018, 9, 1.

[62] G. Wu, C. M. Johnston, N. H. Mack, K. Artyushkova, M. Ferrandon, M. Nelson, J. S. Lezama-Pacheco, S. D. Conradson, K. L. More, D. J. Myers, P. Zelenay, J. Mater. Chem. 2011, 21, 11392.

[63] K. Liu, G. Wu, G. Wang, J. Phys. Chem. C 2017, 121, 11319.

[64] S. Mukherjee, X. Yang, W. Shan, W. Samarakoon, S. Karakalos, D. A. Cullen, K. More, M. Wang, Z. Feng, G. Wang, Small Methods 2020, 1900821.

[65] S. T. Thompson, D. Papageorgopoulos, Nat. Catal. 2019, 2, 558.

[66] W. Wang, Q. Jia, S. Mukerjee, S. Chen, ACS Catal. 2019, 9, 10126.

[67] S. K. Babu, H. T. Chung, P. Zelenay, S. Litster, ECS Trans. 2015, 69, 23.

[68] J. Gostick, Z. Khan, T. Tranter, M. Kok, M. Agnaou, M. Sadeghi, R. Jervis, J. Open Source Soft. 2019, 4, 1296.

[69] M. P. Karthikayini, T. Thirupathi, G. Wang, V. K. Ramani, R. K. Raman, J. Electrochem. Soc. 2016, 163, F539.

This work reports an effective design of catalyst nanostructures and morphologies for atomically dispersed single Co site catalysts through electrospinning cobalt-doped ZIF-8 crystals and selected dual polyacrylonitrile (PAN) and polyvinylpyrrolidone (PVP) polymers. The interconnected porous nanofiber networks with hierarchical architecture are essential to facilitate the mass and charge transfer within electrodes, along with robust three-phase interfaces for the oxygen reduction reaction (ORR). The newly developed single Co site catalyst is highly active and durable for oxygen reduction in proton-exchange membrane fuel cells.

Keywords: Single Co site; oxygen reduction; electrocatalysis; electrospinning; fuel cells

Yanghua He[1], Hui Guo[1], Sooyeon Hwang[1], Xiaoxuan Yang[1], Zizhou He, Jonathan Braaten, Stavros Karakalos, Weitao Shan, Maoyu Wang, Hua Zhou, Zhenxing Feng, Karren L. More, Guofeng Wang, Dong Su, David A. Cullen*, Ling Fei*, Shawn Litster*, and Gang Wu*

Single Cobalt Sites Dispersed in Hierarchically Porous Nanofiber Networks for Durable and High-Power PGM-free Cathodes in Fuel Cells

TOC figure

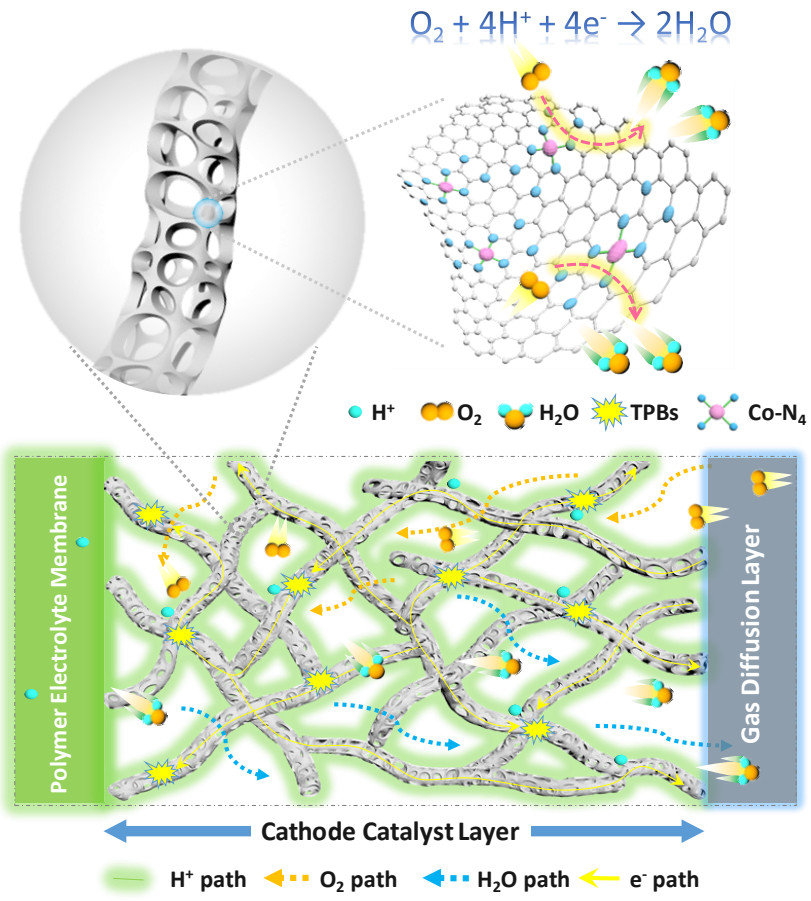

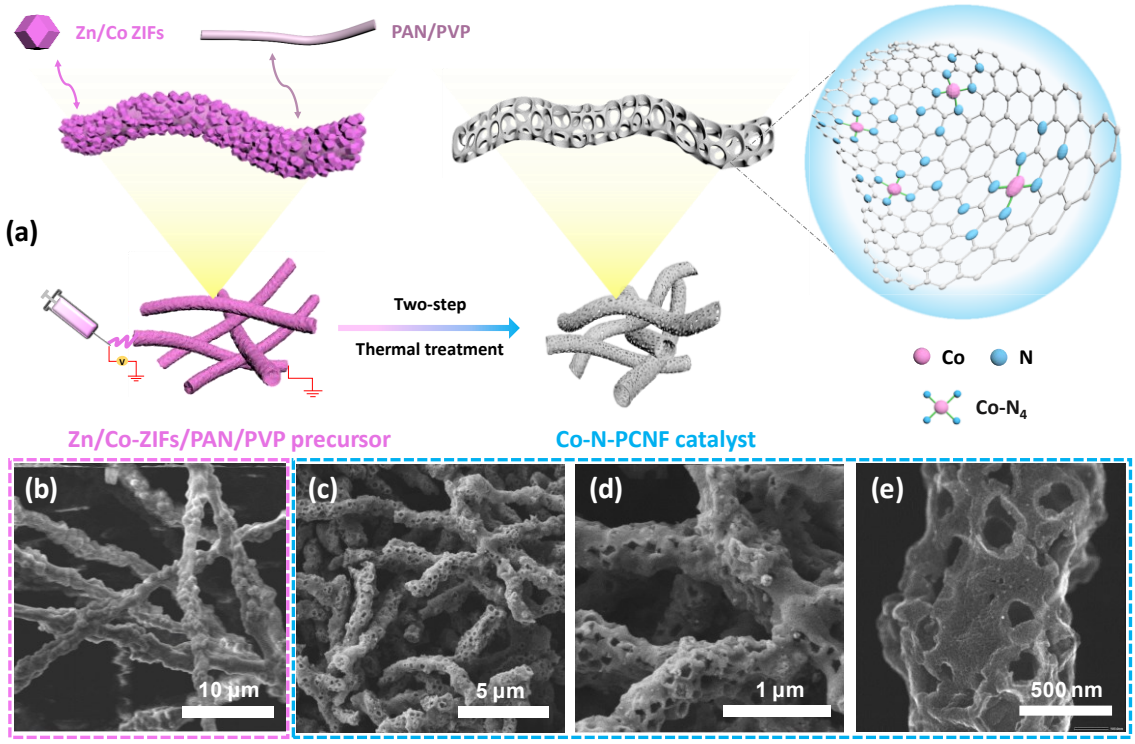

Figure 1. (a) Schematic of the preparation process of Co-N-PCNFs catalysts through co-electrospinning of ZIFs and polymers followed by a two-step thermal activation. (b) Secondary electron (SE) images of the Zn/Co-ZIFs-PAN/PVP precursor and (c-e) the Co-N-PCNF catalyst.

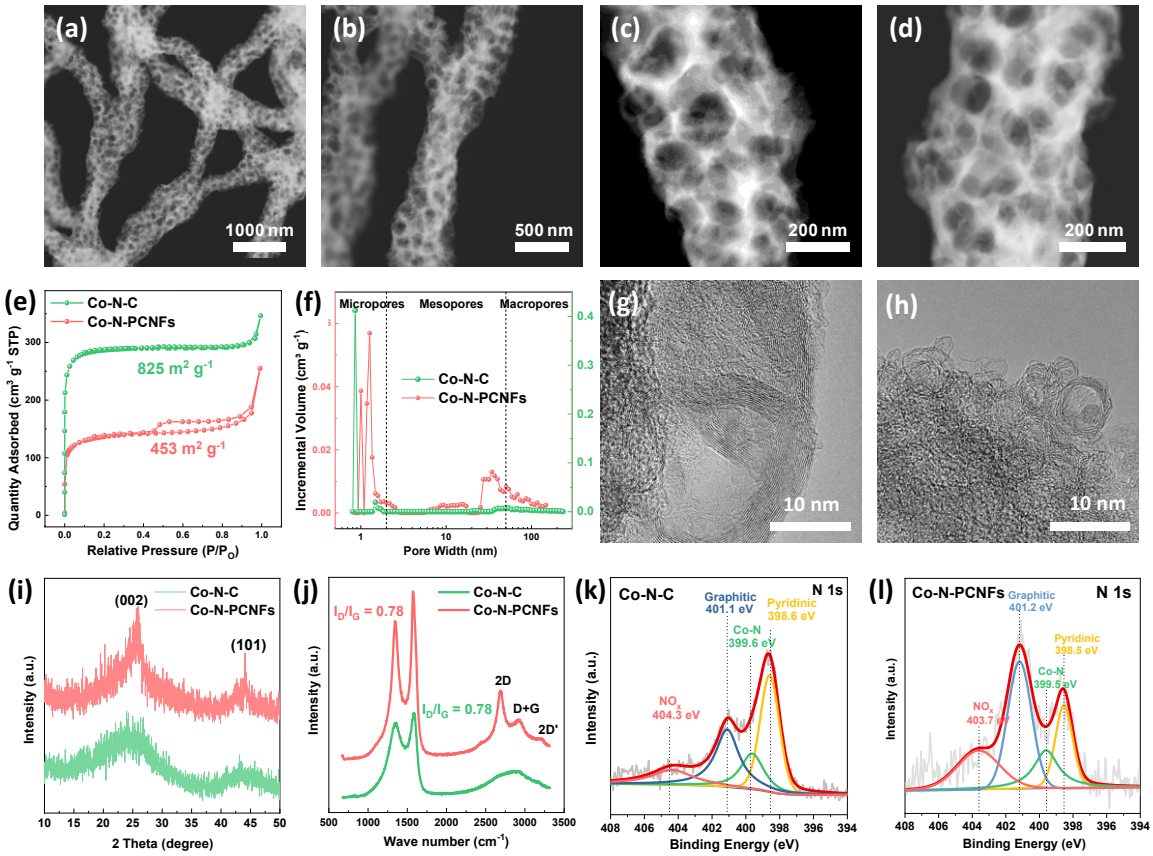

Figure 2. (a-d) HAADF-STEM images of Co-N-PCNFs catalyst. (e) N_2 isothermal adsorption-desorption and (f) pore size distribution for Co-N-C and Co-N-PCNFs catalysts. (g-h) High-resolution TEM images of Co-N-PCNFs with graphitized carbon structure. (i) XRD, (j) Raman, and (k-l) XPS N 1s analysis of Co-N-C and Co-N-PCNFs catalysts.

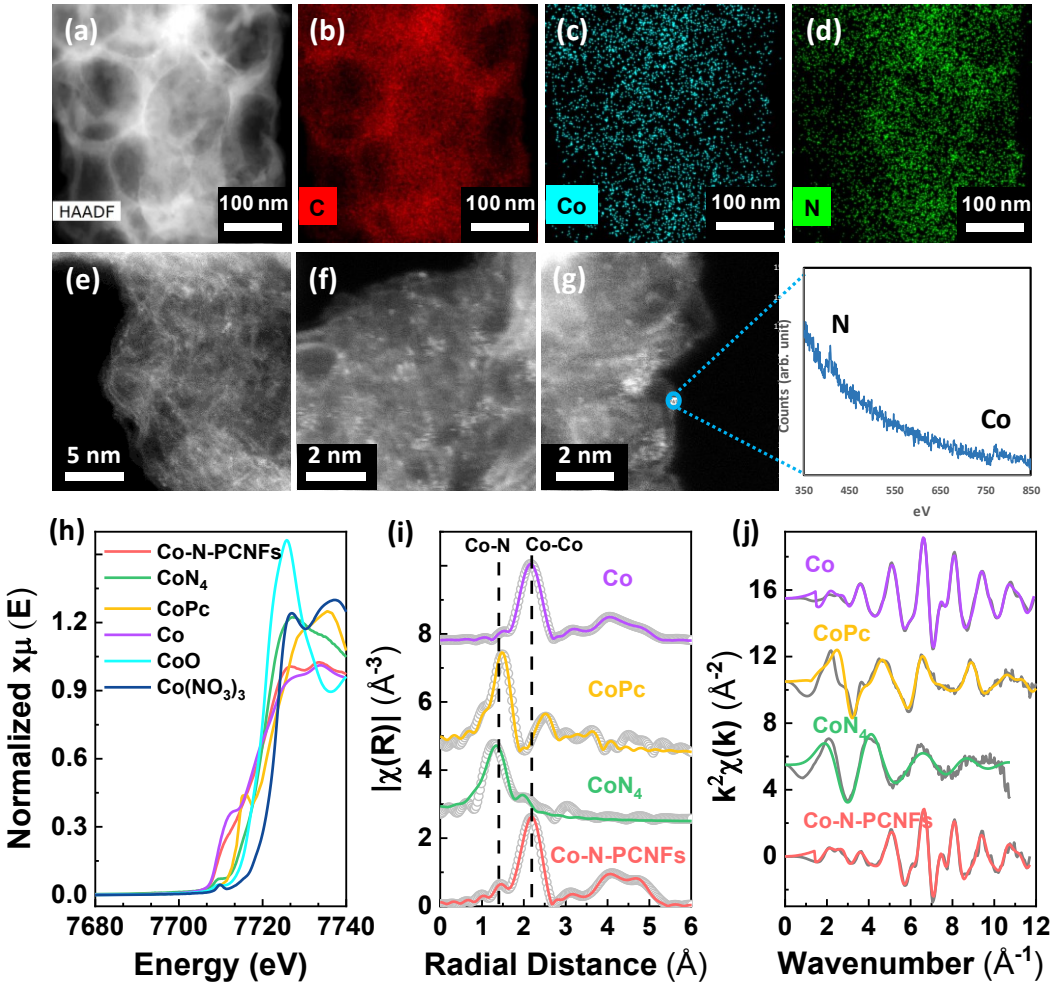

Figure 3. (a-d) HAADF-STEM image and STEM-EDS elemental maps of Co-N-PCNFs sample. (e-g) Aberration-corrected HAADF-STEM images with EELS point spectra of Co-N-PCNFs catalyst. (h-i) Co K edge XANES spectra, fit of the magnitude of the Fourier transform R-space EXAFS (data-circle and fit-red-line), and the fit of the k^2-weighted EXAFS (fit-red-line) of various Co-based samples.

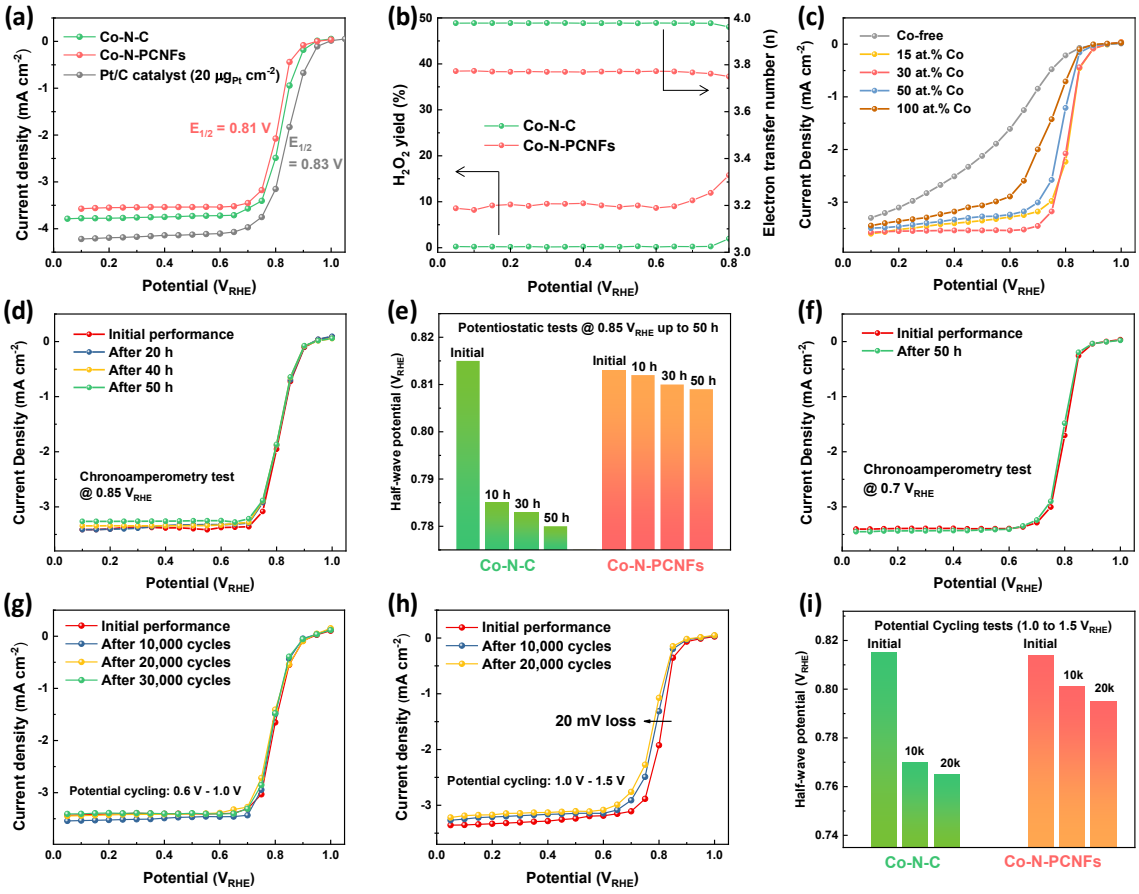

Figure 4. (a) Steady-state ORR polarization plots, and (b) H_2O_2 yield and electron transfer number of Co-N-C and Co-PCNFs catalysts in 0.5 M H_2SO_4 at 25 °C. (c) Co content effect on the ORR activity of Co-N-PCNFs catalysts. Potentiostatic tests (d-e) @ 0.85 V_{RHE} and (f) @ 0.7 V_{RHE}. Potential cycling during (g) low-potential range (0.6 to 1.0 V_{RHE}), and (h-i) high-potential range (1.0 to 1.5 V_{RHE}) for various samples in O_2-saturated 0.5 M H_2SO_4.

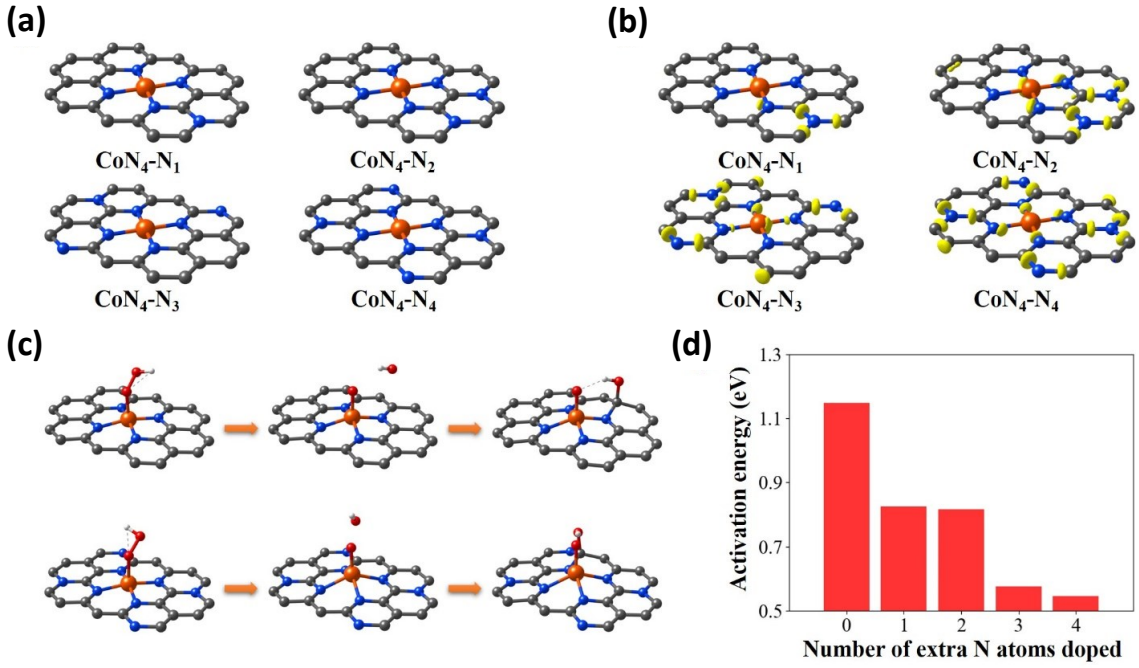

Figure 5. (a) Atomic structures of the N doped Co-N-C catalysts, which were modeled as a graphene layer containing a CoN_4 site and different numbers (*i.e.*, 1 to 4) of graphitic N dopants within a periodic simulation cell. (b) Differential charge distribution map showing the charge accumulation on the C atoms adjacent to N dopants. The charge accumulation is represented by yellow clouds in the figure with the isosurface of 0.02 e/Å^3. (c) Atomic structures are showing the transition states for *OOH dissociation reaction on the CoN_4 site with no extra N doping and the CoN_4-N_4 site with four graphitic N dopants. The initial states (left) and final states (right) were fully relaxed, whereas the transition states (middle) were located using Cl-NEB method. (d) The predicted activation energy for *OOH dissociation reaction on the CoN_4 sites with different numbers of extra graphitic N dopants. In all atomic structures, the gray, blue, orange, red, and white balls represent C, N, Co, O, and H atoms, respectively.

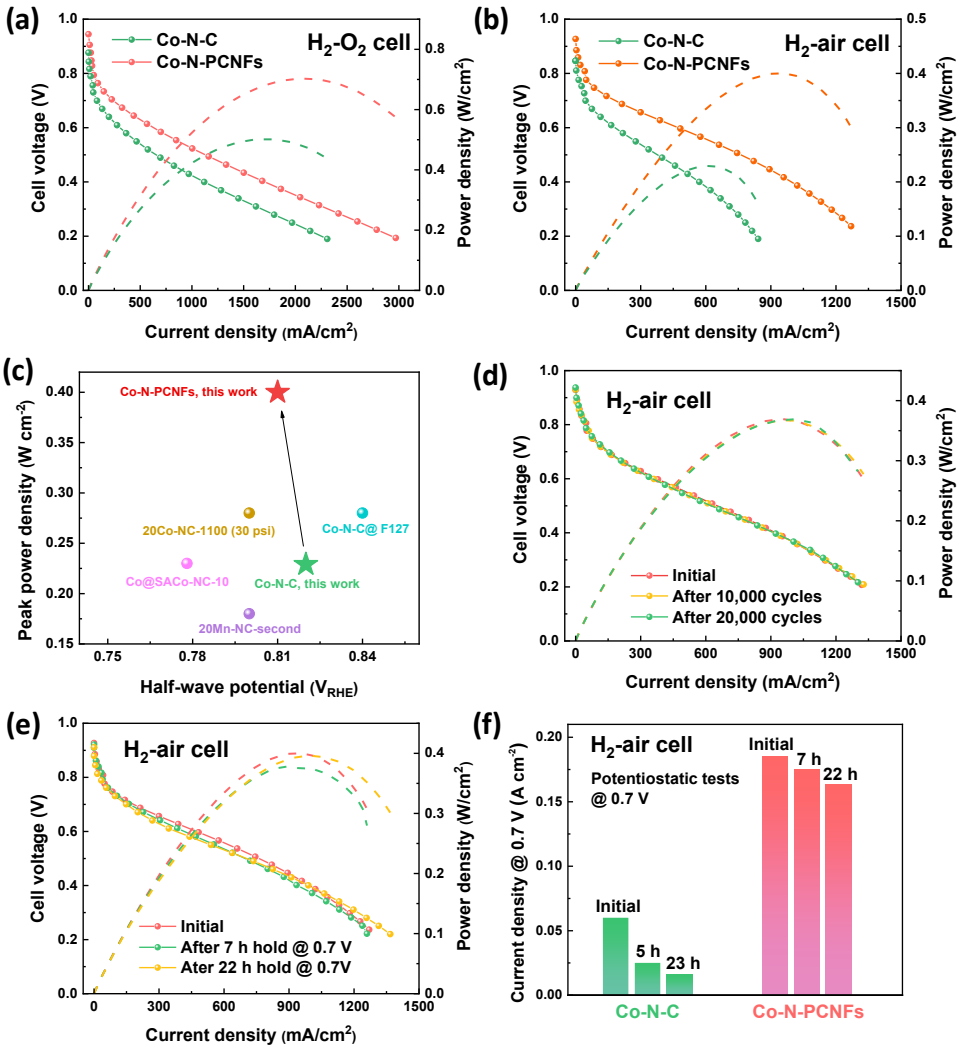

Figure 6. (a-b) Performance comparisons for Co-N-C and Co-N-CNFs cathode catalysts in both H_2-O_2 and H_2-air cells. (c) ORR activity and MEA performance comparison between Co-N-PCNFs and the literature reported Co-based catalysts[15, 36, 49, 69]. Fuel cell stability tests for Co-N-CNFs cathode catalyst through (d) voltage cycling between 0.6 to 0.95 V, and (e-f) potentiostat test @ 0.7 V in an H_2/air fuel cell. Cathode catalyst loading: ~4.0 mg cm^{-2}. Cell temperature: 80°C; flow rate H_2/O_2 or air 200/1000 sccm. 100% relative humidity. 1.0 bar H_2/O_2 or air. Nafion 212.

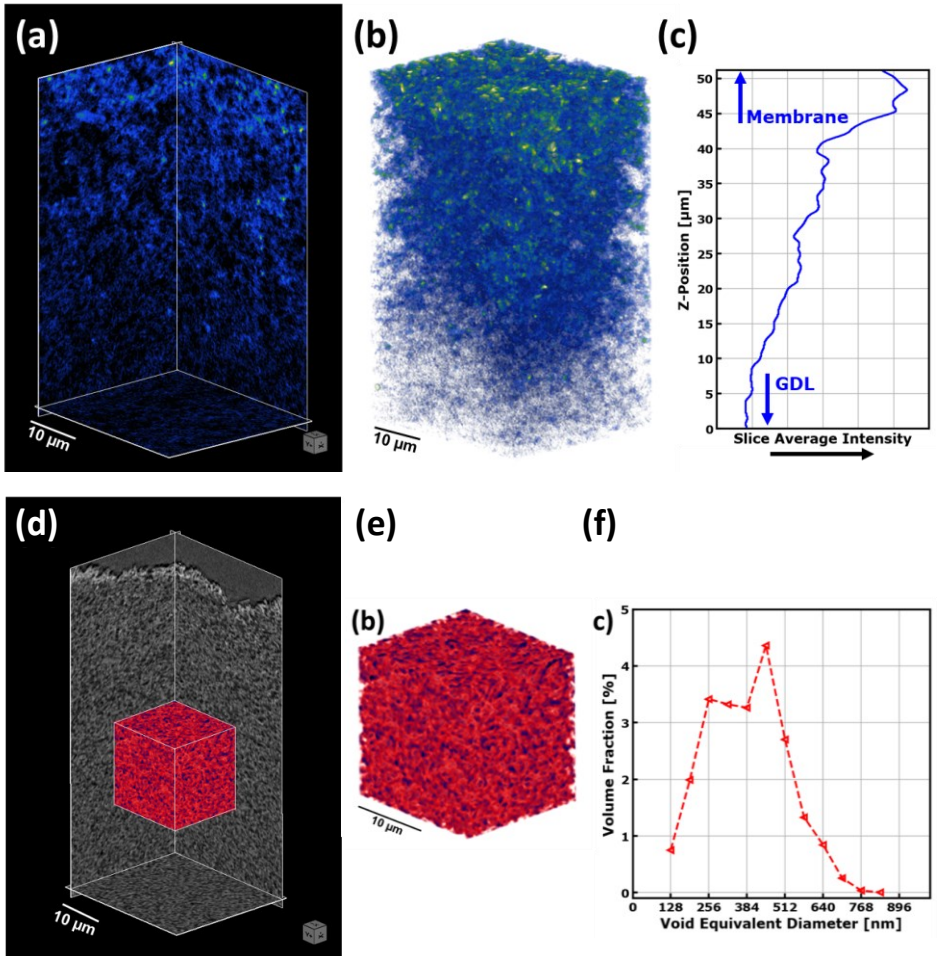

Figure 7. Imaging of the Cs^+ stained ionomer contrast by absorption contrast nano-CT. (a) Virtual slices, (b) volume rendering, and (c) average in-plane slice intensity versus position through the thickness. Zernike phase contrast imaging of the pore-solid structure in the Co-N-PCNFs cathode. (d) Slice view, (e) sub-volume rendering, and (f) void equivalent diameter distribution within the sub-volume.